Cronfa - Swansea University Open Access Repository

_____

This is an author produced version of a paper published in :
Nanotechnology

_____

_____

_____

Factors that determine and limit the resistivity of high-quality individual ZnO nanowires

Factors that determine and limit the resistivity of high-quality individual ZnO nanowires

Alex M Lord[1]**, Thierry G Maffeis**[1]**, Alex S Walton**[2,7]**,
Despoina M Kepaptsoglou**[3]**, Quentin M Ramasse**[3]**, Michael B Ward**[4]**,
Jürgen Köble**[5] **and Steve P Wilks**[6]

[1] Multidisciplinary Nanotechnology Centre, College of Engineering, University of Swansea,
Singleton Park, SA2 8PP, UK
[2] School of Physics and Astronomy, University of Leeds, Leeds, LS2 9JT, UK
[3] SuperSTEM Laboratory, SFTC Daresbury Campus, Keckwick Lane, Daresbury, WA4 4AD, UK
[4] Institute for Materials Research, University of Leeds, Leeds, LS2 9JT, UK
[5] Omicron Nanotechnology GmbH, Limburger Straße 75, D-65232 Taunusstein, Germany
[6] Multidisciplinary Nanotechnology Centre, Department of Physics, College of Science, University of
Swansea, Singleton Park, SA2 8PP, UK

E-mail: s.p.wilks@swansea.ac.uk

Abstract
Knowing and controlling the resistivity of an individual nanowire (NW) is crucial for the production of new
sensors and devices. For ZnO NWs this is poorly understood; a 10^8 variation in resistivity has previously been
reported, making the production of reproducible devices almost impossible. Here, we provide accurate
resistivity measurements of individual NWs, using a four-probe scanning tunnelling microscope (STM),
revealing a dependence on the NW dimensions. To correctly interpret this behaviour, an atomic level
transmission electron microscopy technique was employed to study the structural properties of the NWs in
relation to three growth techniques: hydrothermal, catalytic and non-catalytic vapour phase. All NWs were
found to be defect free and structurally equivalent; those grown with a metallic catalyst were free from Au
contamination. The resistivity measurements showed a distinct increase with decreasing NW diameter,
independent of growth technique. The increasing resistivity at small NW diameters was attributed to the
dominance of surface states removing electrons from the bulk. However, a fundamental variance in resistivity
(10^2) was observed and attributed to changes in occupied surface state density, an effect which is not seen with
other NW materials such as Si. This is examined by a model to predict the effect of surface state occupancy on
the measured resistivity and is confirmed with measurements after passivating the ZnO surface. Our results
provide an understanding of the primary influence of the reactive nature of the surface and its dramatic effect
on the electrical properties of ZnO NWs.

S Online supplementary data available from stacks.iop.org/Nano/24/435706/mmedia

(Some figures may appear in colour only in the online journal)

[7] Present address: Interdisciplinary Nanoscience Center (iNano), Aarhus
University, Gustav Wieds Vej 14, DK-8000 Aarhus C, Denmark.

1. Introduction

Devices based on nanowires (NWs) take advantage of the
exotic properties of materials at low dimensions. For instance,
the enhanced surface-to-volume ratio can provide superior
surface sensitivity, along with novel electronic and optical

characteristics that arise due to quantum confinement. NWs composed of ZnO are of significant interest as they have advantages over other mainstream semiconductor NWs such as Silicon and GaN. For example, the wide direct bandgap can produce lasing at room temperature [1], the piezoelectric characteristics can be used for energy harvesting [2] and the high surface sensitivity, combined with biocompatibility, for gas or bio sensing [3]. However, the dependence of these properties on the dimensions of the NW, the surface termination of the NW and any interface that the NW forms, is still not fully understood and remains a field of great debate [4]. A fundamental challenge is the difficulty in accurately measuring the electrical resistivity of ZnO NWs. This was initially highlighted by Schlenker *et al* who reported NW resistivity spanning almost eight orders of magnitude, from 10^3 to 10^{-5} Ω cm [5], and experimental evidence [5–8] to this day still covers a range of at least 10^{-2}–10^3 Ω cm. Such a large variation in resistivity, for similar ZnO NWs, currently makes the design of manufacturable devices unfeasible and uncovering its origin is the main focus of this paper.

There are several reasons why such a vast range in resistivity has been reported. Firstly, depending on the particular NW growth technique and the conditions employed, it is possible that differences in crystallographic structure, doping concentration or surface architecture/chemistry may occur. Secondly, ZnO has no natural passivation layer on its surface, making it highly susceptible to changes in environment (storage or measurement) due to random adsorbates [9–12] that can lead to variability in the occupied surface state density. Finally, there can be significant reproducibility errors introduced by the technique that is used to measure the resistivity at the nanoscale, namely the four-point-probe (FPP). This method presents three challenges when working at the nanoscale: (a) multiple processing steps involving lithography [6, 13] or ion-beam deposition [7, 8] are required to produce a sample suitable for FPP, these can alter the intrinsic NW surface properties, (b) each resistance measurement undertaken during the FPP experiment requires a bespoke structure to be fabricated using a different NW each time, and (c) these measurements are conducted in a variety of environments that will significantly affect the measurement. To resolve these issues we report here resistivity measurement of 40 ZnO NWs in a controlled environment without the need for any sample processing, using an ultra-high vacuum (UHV) four-probe scanning tunnelling microscope (STM). The NWs were grown by three different techniques that are popular in the literature. To accurately interpret the results, structural studies were conducted in parallel using techniques such as transmission electron microscopy (TEM) and high resolution high angle annular dark field (HAADF) imaging to examine differences that may result from each growth methodology. For example, a major concern for some NW materials, produced by the catalytic vapour–liquid–solid (VLS) method, is the contamination of the NW bulk or surface with residual Au catalyst atoms. This has been shown to hinder the electrical properties of the materials, particularly silicon [14], GaAs [15] and InAs [16] due to the introduction of detrimental acceptor or donor levels affecting the NW resistivity. For ZnO produced using this growth method, the possibility of catalyst contamination has not been previously resolved. Along with other process parameters, the inclusion of foreign atoms can locally alter the crystal structure, subsequently changing the NW properties such as the free carrier concentration [17]. However, the NWs produced, measured and reported here show no structural differences due to the different growth techniques and form high-quality NWs. Furthermore, the electrical measurements reveal a trend of increasing resistivity as the NW diameter is reduced which is explained by a model that considers a surface depletion layer associated with trapped charge on the reactive ZnO surface. Variations in the surface state density, as a result of random absorption of species on the surface, produces a fundamental spread in resistivity that explains the highly sensitive nature of ZnO nanostructures. This conclusion is confirmed by exposing NWs to ethanol, which is a known surface state passivant for ZnO. The effect of the ethanol reduces the NW resistivity to an almost common datum independent of NW diameter.

2. Experimental details

2.1. NW growth

Vapour-phase catalytic NWs were grown on an α-Al$_2$O$_3$ wafer using a solid ZnO and C source evaporated in a controlled atmosphere in a tube furnace [18]. Catalysed growth occurred at $\sim$900 °C with a flow of 49 sccm Ar, 1 sccm O$_2$ at 30 mbar chamber pressure using a thin ($\sim$6 nm) Au layer deposited by plasma sputtering prior to growth. Vapour-phase NWs without a catalyst were grown on a bare chemically roughened α-Al$_2$O$_3$ substrate [19] with a furnace temperature of 1050 °C, a local growth temperature of $\sim$600 °C and an atmosphere at 1.6 mbar with a flow of 100 sccm Ar/10 sccm O$_2$. Finally, hydrothermal NWs were synthesized from a precursor solution of ZnCl$_2$ (0.2 g) and Na$_2$CO$_3$ (20 g) ($\sim$4.72 M) in distilled water (50 ml) sealed in a stainless steel autoclave, then heated and maintained at 140 °C for 12 h [20]. The hydrothermal NWs were centrifuged, re-diluted in distilled water and centrifuged again, this process was repeated a number of times to remove any traces of the growth base before finally drying in vacuum.

2.2. Measurement substrate fabrication

NWs were directly transferred to Au patterned insulating SiO$_2$ substrates. Prior to transfer, linear photoresist tracks of 10–20 μm in width and spacing of 10 or 30 μm were formed on the SiO$_2$ substrate before Au was deposited and the resist lifted off. This process formed Au tracks covering $\sim$5 mm^2 over the substrate with a connecting electrical contact pad at either end. Substrates were then solvent cleaned and crucially Piranha etched to remove any traces of the patterning process. The vapour-phase NWs were then transferred by mechanical contact between the growth substrate and the patterned SiO$_2$ substrate. We found that this process did not affect the resistivity (supplementary figure S1 available at

stacks.iop.org/Nano/24/435706/mmedia). The hydrothermal NWs were transferred by suspending the NWs in IPA and immediately drop casting on the measurement substrate, followed by drying in air. IPA was chosen as the dispersion solvent as it does not have any effect on the NWs over short periods of exposure [21]. To confirm surface state activity, hydrothermal NWs were dispersed into ethanol (200 proof) before dispensing the mixture on the measurement substrates, followed by drying in air.

2.3. Nanoprobe measurements

The Omicron UHV Nanoprobe comprises four individual tungsten probes guided by a Gemini SEM column. By guiding the four STM tips with the SEM it is possible to form reversible, non-destructive electrical contacts to an individual nanostructure. The electrical measurements were conducted with a Keithley 2601 source metre with a measurement range of picoamp to Amp and HP multiplexer 3488A was used to switch between probes. Samples were loaded into the nanoprobe and the loadlock was pumped overnight. Samples were transferred to the main chamber and it was essential that the tips were cleaned *in situ* under UHV by current annealing to remove oxides and contaminants. The tracks were used for a tunnelling current feedback approach to position the probe tips of the nanoprobe at the correct height near the NW before making contact, then measurements were taken. Tips were placed on the NWs and contacts were tested by *I–V* sweeps between probes. With suitable contact at each tip further measurements were completed.

2.4. TEM characterization

Samples were prepared for TEM analysis by rubbing a carbon support film (holey carbon film on 400 mesh Cu, Agar Scientific) on top of the NW array on the substrate. FEI Tecnai TF20 FEGTEM operated at 200 keV equipped with a selected area electron diffraction (SAED) aperture and an Oxford Instruments INCA 350 energy dispersive x-ray spectroscopy (EDX) system/80 mm X-Max SDD detector.

2.5. STEM characterization

High resolution high angle annular dark field (HAADF) imaging was carried out in a Nion UltraSTEM100 scanning transmission electron microscope (STEM) operated at 100 keV primary beam energy [22]. The probe-forming optics, corrected for aberrations up to fifth order, were configured to provide ∼100 pA of beam current with a 31 mrad beam convergence semi-angle, for an estimated probe size of 0.8 Å. The inner and outer radii of the HAADF detector were calibrated at 79 mrad and 195 mrad, respectively.

2.6. HAADF simulations

Image simulations were performed using the multi-slice method as implemented in the QSTEM Software Suite [23], using measured experimental parameters for the probe convergence and detector geometry and aberration coefficients.

The chromatic aberration coefficient was set to $Cc = 1.3$ mm and the native energy spread of the cold field emitter of the instrument is $\Delta E = 0.30$ eV. Thermal diffuse scattering effects were simulated using a total of 15 frozen phonons in the simulations. Finally, partial coherence effects (due to finite probe size or instabilities for instance) were incorporated in the simulations by convolution of the simulated images with a Gaussian of 0.08 Å full-width at half-maximum. Slabs of ZnO of various thicknesses were created for the simulations aligned along the [01$\bar{1}$0] zone axis and with a flat entrance and exit surface. Single Au atoms were then substituted for Zn atom at various depths within the slab (along the beam propagation direction), without any additional relaxation of the lattice.

3. Results and discussion

To overcome the reliance on the complicated processing steps that are required to fabricate the structures necessary to measure the resistivity of individual NWs, experiments were conducted using a nanoprobe instrument, containing four independent STM probe tips that can be manipulated at the nanoscale to contact a single NW, under the navigation of a scanning electron microscopy (SEM) column. The UHV nanoprobe chamber provides a stable environment for measurements on as-grown samples where no sample processing is required. Here non-destructive contact is made directly to the NWs using the four moveable probes so that several resistance measurements can be performed on a single NW to reveal its true resistivity. Multiple 4-probe measurements were taken on 40 NWs of varying diameter (16 catalysed, 14 non-catalysed and 10 hydrothermal). After growth the NWs were directly transferred to a Si wafer, previously capped with ∼300 nm of SiO$_2$ and patterned with Au tracks. The tracks were used for a tunnelling current feedback approach to position the tips of the nanoprobe at the correct height near the NW before making contact. Great care was taken to clean the patterned tracks prior to NW transfer, including an intense Piranha etch, without which, heavy beam deposition due to residual organic material from the formation of the tracks was apparent during *in situ* SEM imaging. When this occurred, very low currents (nanoamps) were measured through the NWs. This provides an indication of the problems that can be encountered when using semiconductor fabrication techniques such as electron beam lithography. The NW samples were placed into the nanoprobe via a loadlock, which was pumped overnight prior to transfer into the main chamber where the tungsten tips were delicately positioned onto the structures using the fine-piezo controls which avoided any damage. With a suitable Ohmic contact at each tip, a FPP measurement was taken with current sourced between the outer tips and the voltage drop measured between the inner probes. An example of the experimental configuration is shown in figure 1(a). On each NW, multiple FPP measurements were performed at various inner probe separations: a typical result of the experiment performed on a single NW at room temperature is shown in figure 1(b); as previously mentioned, using patterned contacts, a new sample
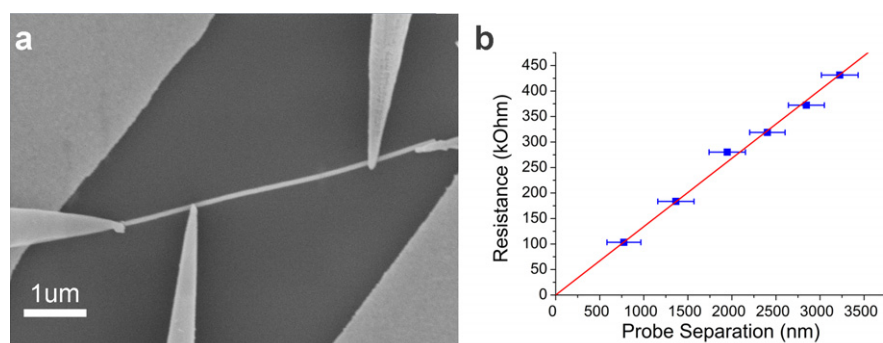
Figure 1. (a) *In situ* top-down SEM image from the nanoprobe showing the four-probe tips on a ZnO NW lying flat on insulating SiO₂. (b) Plot of the four-probe resistivity measurements with multiple probe separations showing the good fit to Ohm's law (red line), the gradient reveals the intrinsic resistivity of the NW (0.078 Ω cm), the error bars are due to the width of the probe tips masking the exact contact position.

and NW would be required for each data point in figure 1(b). The probe tips form a contact area that is much smaller than the NW radius, overcoming the problem of large electrodes which can allow equalization of charge carriers [24], hence giving a true FPP measurement. Assuming a cylindrical NW the resistivity ρ (Ω) can be calculated from the best fit of the resistance-separation graph (figure 1(b)) using the gradient dR/dL, where R is the four-probe resistance, L is the probe separation (L) using

$$\rho = \frac{dR}{dL} A \qquad (1)$$

and where A is the NW cross sectional area estimated from the measured diameter (see supplementary figure S2 available at stacks.iop.org/Nano/24/435706/mmedia). The source voltage was typically ±0.1 V up to ±1 V for currents in the microamp range depending on NW resistivity. Usually at least five different separations of the inner probes were used for each NW, depending on the overall length. The individual current–voltage curves for each FPP measurement showed a linear behaviour, regardless of the NW size, and the resistance scaled with length as expected from Ohm's law.

The FPP resistivity measurements of each NW, from the catalysed (only NWs with distinct Au tips were measured), non-catalysed and hydrothermal growth methods are shown in figure 2, as a function of NW diameter. The values for the resistivity range from 0.02 to 2 Ω cm, for diameters between 40 and 160 nm. The measurements are in good agreement with a previous nanoprobe measurement on a ZnO NW by Lin *et al* who reported a resistivity of 0.24 Ω cm [25]. From figure 2, several observations can now be made from the distribution in resistivity values: (i) there is no clear correlation between the resistivity and the growth technique used; (ii) there is an overall trend of increasing resistivity with decreasing NW width; and (iii) there appears to be an inherent variability, or scatter, in the measured conductivity at each NW diameter, which also increases as the NW diameter diminishes.

Variations in NW resistivity can result from sources such as crystallographic defects or stoichiometric differences, including grain boundaries, dislocations and point defects, Zn interstitials and O vacancies, that affect doping levels, catalyst
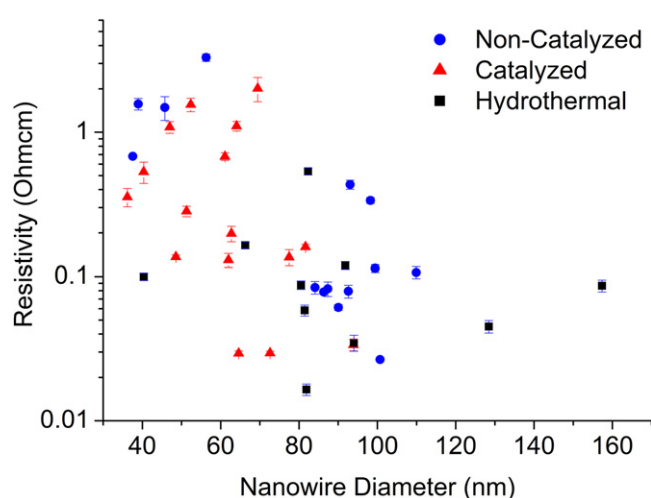
Figure 2. Resistivity-nanowire diameter graph of 16 catalysed (red), 14 non-catalysed (blue) and 10 hydrothermal (black) NWs depicting a general increasing trend in resistivity as the diameter decreases. Error bars arising in the diameter measurement from the SEM resolution of ±2.5 nm are omitted for clarity. The error bars in resistivity show the standard error in the ordinary least squares algorithm of MATLAB.

or impurity contamination during growth or modification of surface properties, particularly for systems having large surface-to-volume ratios. Resistivity is highly dependent on carrier concentration, but for ZnO the source of the native n-type doping is still debated and mainly concerned with possible sources such as Zn interstitials, O vacancies or H, incorporated during or after growth [26]. Variations of such point defects and impurities could result in a range of carrier densities from NW to NW and would be expected to be prominent between different growth techniques resulting in a spread in NW resistivity. However, no clear trend associated with each growth method can be identified for the 40 NWs measured here, aside from the collective increase in resistivity as the NW diameter diminishes. When a distinct relationship with diameter is present it indicates a strong surface influence on the conduction properties, possibly creating the effect in (ii). However, the spread in the measured property, point (iii),
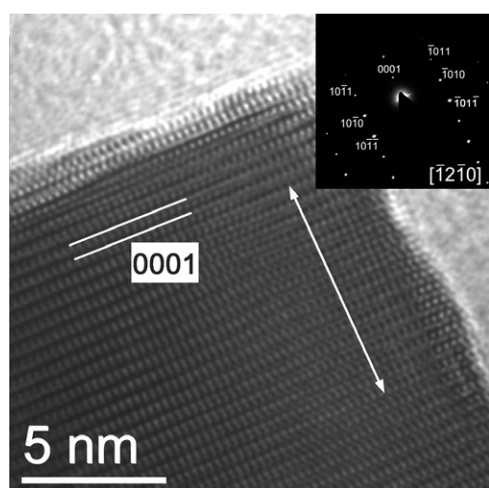
Figure 3. TEM lattice imaging revealed the (0001) lattice spacing of the NWs, this hydrothermal example is typical of the three growth techniques, and the inset shows the SAED pattern displaying single crystal quality and the [0001] growth direction. The diffraction patterns of each growth type confirmed the same wurtzite unit cell with an approximate lattice spacing of 5.2 Å, 2.9 Å and 3.3 Å for the (0001), $\{10\bar{1}0\}$ and $\{11\bar{2}0\}$ planes, respectively.

could equally stem from the structure of the NWs. The NWs were grown by three distinct methods that could introduce variations in composition and crystal structure; therefore, it was necessary to examine each NW type in detail and characterize any differences that exist.

Initial structural and compositional investigations were performed using TEM operated at 200 keV and equipped with a selected area electron diffraction (SAED) aperture and an energy dispersive x-ray spectroscopy (EDX) detector. This revealed that all three NW types possessed the same wurtzite crystal structure with no defects or substantial elemental variation: as an example of a typical result, the TEM image of a hydrothermal sample is shown in figure 3 and the corresponding EDX analysis in supplementary figure S3 (available at stacks.iop.org/Nano/24/435706/mmedia). No substantial variations in the surface morphology were detected on the measured NWs indicating, as far as these techniques can tell, the NWs grown by the hydrothermal and vapour-phase methods were equivalent, with growth along [0001] and no lattice or compositional variation.

However, limitations in the techniques mean that they do not possess the sensitivity to uncover atomic anomalies that may arise, particularly in vapour-phase NWs grown with the aid of Au catalyst. Aberration-corrected HAADF in a dedicated scanning transmission electron microscope (STEM) can reveal the presence of large Z-number atoms even in challenging host materials [15] and uncover structural details hidden within the depths of the material. Point defects in the NW bulk are a particular hindrance which can only be directly investigated by atomic-scale electron microscopy [27].

Catalysed and non-catalysed NWs of diameters ranging from 15 to 60 nm were directly transferred to a holey carbon coated TEM grid and inspected with HAADF imaging in an aberration-corrected Nion UltraSTEM, operated at
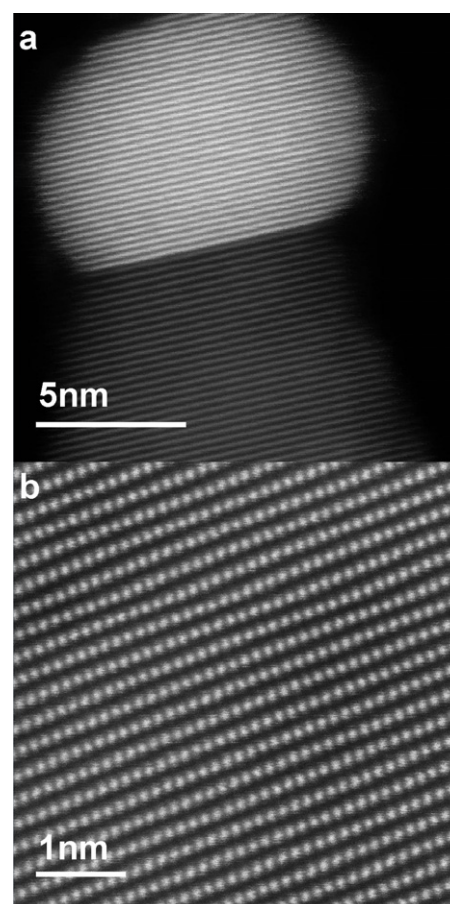
Figure 4. HAADF–STEM images of a catalysed ZnO NW transferred directly to a TEM grid. (a) The regular pattern of the atomic *c*-plane lattice of Zn atoms is apparent along with the lattice of the single crystal Au catalyst. (b) High magnification HAADF imaging where the $\sim Z^{1.7}$ relationship with intensity would reveal Au atoms as high contrast bright spots. Thorough searching revealed no Au atoms interstitially or within the Zn atomic columns.

100 keV primary beam energy with an estimated probe size of 0.8 Å [21]. The non-catalysed NWs that were grown with only the substrate roughness as nucleation sites served as a control sample. A typical HAADF image of a catalysed NW is shown in figure 4(a). As an aside to the comparison of the NW types, it is interesting to note that figure 4(a) shows a distinct single crystal Au catalyst particle tip in lattice alignment with the ZnO crystal. This suggests an epitaxial relationship was present during growth which can only occur if the Au remains solid throughout [28]. Furthermore, the Au lattice planes display the {111} spacing of 2.35 Å consistent with the Au $(11\bar{1}) \parallel$ ZnO(0002) interface described by Brewster *et al* [29]. It is unlikely that alloying of Zn and Au occurred [28, 29]; as confirmed by lattice spacing measurements (comparable to pure Au crystal) and EDX detecting no presence of Zn in the growth tip, (supplementary figure S2c available at stacks.iop.org/Nano/24/435706/mmedia). Additionally, a disordered growth meniscus is found around the edge of the Au particles near the ZnO interface (evidence of this is displayed in supplementary figure S4 available at stacks.iop.org/Nano/24/435706/mmedia). This feature, along with no detectable
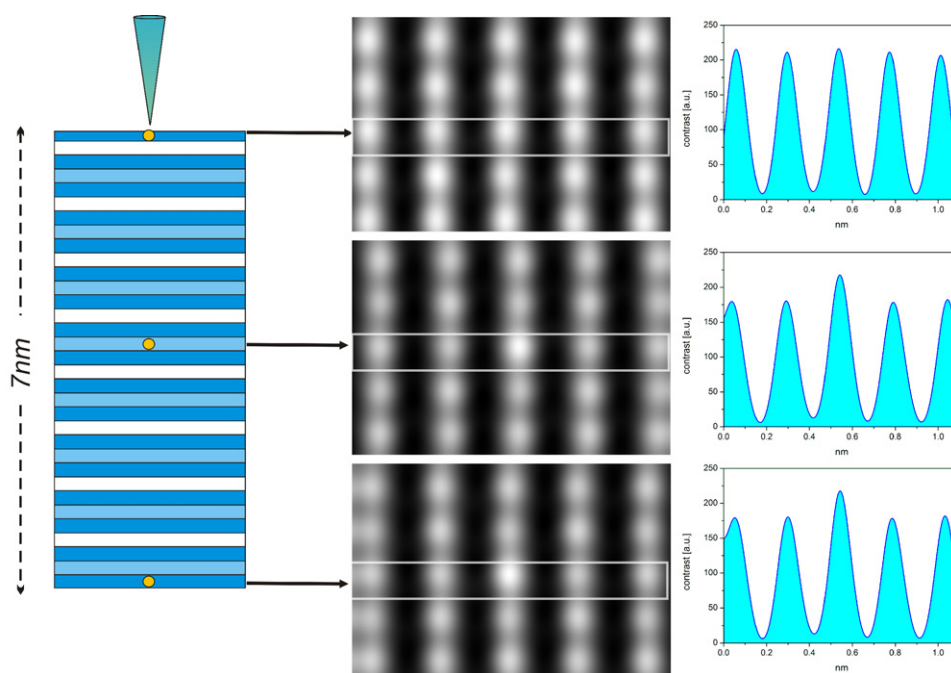
Figure 5. HAADF image simulations of a ZnO slab 7 nm thick, with one Au impurity atom placed at the entrance surface, middle or exit surface of the slab. The graphs show the expected excess intensity created by the single Au atom within a Zn column reaches a maximum of ∼20% when located in the middle or near the exit surface.

alloying and an epitaxial relationship between the catalyst and NW, provides further evidence for vapour–solid–solid growth in ZnO NWs that is driven by diffusion of Zn around the catalyst surface [28–30].

High resolution HAADF images (figure 4(b)) show the Zn columns in a region near to the side of the length of the NW structure. The NWs tended to naturally lie on a side facet of the hexagonal crystal: a number of images were therefore acquired with the beam travelling down the [01$\bar{1}$0] zone axis. In these 'Z-contrast' images, the intensity scales approximately as the square of the average atomic weight number of the imaged material as $Z^{1.7}$ [31]. The large atomic number difference between Au ($Z = 79$) and the ZnO matrix ($Z = 30$ and 8 for Zn and O, respectively) should therefore offer favourable conditions for detecting impurity Au atoms within the NWs, which if present are expected to generate a clear image intensity increase. No such contrast variation was detected in any region of any of the NWs imaged in this study, providing a reasonable indication that our NWs are devoid of any catalyst impurity. However, it is well-known that channelling along atomic columns can reduce the visibility of substitutional or interstitial impurities, sometimes to a point where they cannot be detected in the resulting HAADF images [15, 32].

To analyse whether this may have adversely affected the imaging it was possible to perform multi-slice simulations using the QSTEM Software Suite [23] with measured experimental parameters for the probe convergence, detector geometry and aberration coefficients. To simulate the ZnO NWs, slabs of various thicknesses were created aligned along the [01$\bar{1}$0] zone axis and with a flat entrance and exit surface. A single Au atom was then substituted for a Zn atom at various

depths within the slab (along the beam propagation direction), without any additional relaxation of the lattice. The atomic arrangement of the ZnO presented to the beam along with a substitutional Au atom is depicted in supplementary figure S5 (available at stacks.iop.org/Nano/24/435706/mmedia). This model provides a good estimate of the additional contrast heavy Au atoms are expected to generate when located within the host matrix. In the conditions used for our experiments, the presence of a single Au atom in the bulk or near the exit surface of a 7 nm thick slab of ZnO would generate a contrast increase of ∼20% as shown in figure 5, for a thicker slab of 14 nm an excess intensity of ∼15% can be expected when near the exit surface (see supplementary figure S6 available at stacks.iop.org/Nano/24/435706/mmedia).

These imaging conditions should have therefore allowed the detection of Au impurity atoms even when on zone axis, in particular on the beam exit surfaces or near edges of the NWs where the overall material thickness is reduced compared to its bulk. It is possible to reveal Au atoms in these locations with aberration-corrected instruments because of the large probe convergence angles (here 31 mrad semi-angle) that enable depth-slicing techniques which exploit the reduced depth of field (2–4 nm) to locally image impurities buried within the sample depth, in particular at point defects [14, 27, 33]. Using this technique the NWs were thoroughly searched for point defects including those that maybe associated with Au atoms; sectioning the structures with through-focal imaging series, recorded along the NWs zone axis, showed no trace of impurities or defects confirming the high quality and purity of the crystals (supplementary figure S7 available at stacks.iop.org/Nano/24/435706/mmedia). It should be noted that the detection of O vacancies and low
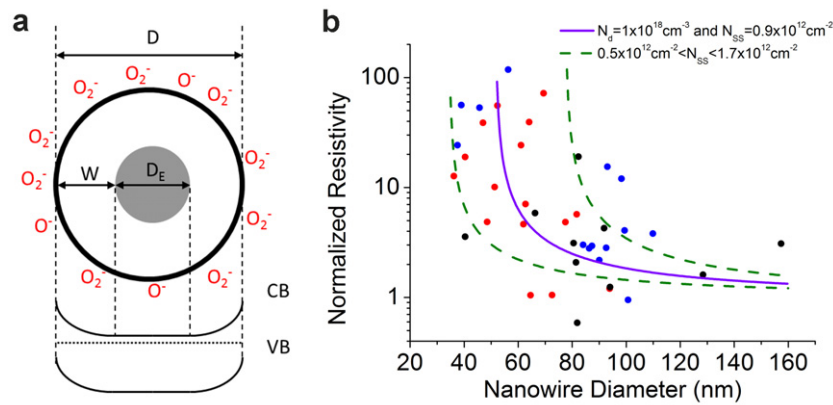
Figure 6. (a) Schematic diagram of a ZnO NW cross section with oxygen ions on the surface depleting the bulk of charge carriers resulting in surface band bending and a reduced conductive core (grey). (b) Plot of the resistivity normalized to 0.028 Ω cm against the NW diameter for each NW type and the model parameters of $N_d = 1 \times 10^{18}$ cm^{-3} and $N_{ss} = 0.9 \times 10^{12}$ cm^{-2} that describe the experimental relationship with diameter (purple). Also shown is the range of values $N_{ss} = (1.1 \pm 0.6) \times 10^{12}$ cm^{-2} that are required to express the experimental data spread (green).

Z-number elements such as H in the ZnO matrix are beyond the detection limits of the techniques used here. The difficulty in detecting these stoichiometric or compositional variations makes the specific determination of the source of ZnO n-type carriers very difficult to pin-point [26]. However, using the technique of aberration-corrected HAADF–STEM it is possible to uncover previously unseen atomic deformations and impurities in single crystals with advanced knowledge of the electron interactions and using techniques such as those popularized by Bar-Sadan *et al* of tilting the structure away from channelling conditions (from the zone axis) which can improve the visibility of impurities in unfavourable materials [15]. Using this technique even with an atomic weight ratio as low as $Z_{Au}/Z_{Ga} = 2.55$ or $Z_{Au}/Z_{Zn} = 2.63$ the detection of single Au atoms in a NW is still possible. This experimental technique (supplementary figure S8 available at stacks.iop.org/Nano/24/435706/mmedia) combined with the simulations confirm that no isolated Au atoms, clusters or bulk Au diffusion was present in any catalysed NW. All recorded images were in fact similar to those taken of non-catalysed NWs (supplementary figure S9 available at stacks.iop.org/Nano/24/435706/mmedia), and no irregularities between the growth types were found throughout the microscopy analysis.

The structural and compositional analysis of the NWs is in excellent agreement with the electrical measurements and confirms the equivalence of the vapour-phase and hydrothermally produced NWs in terms of crystal quality and electrical properties; ZnO NW resistivity for the three different methods is indistinguishable and shows no growth specific trends. This is an important result that has been masked by the large variability in previous measurements. However, to have confidence in this finding, the origin of points (ii) and (iii) must be clarified as no distinction between NWs can be made with the probing techniques used so far.

There are other influences that must be considered to explain the spread in resistivity that has been measured. Quantum mechanical effects can be ignored as the measured wires are not small enough to exhibit such behaviour in

ZnO. The work of Björk *et al* [34] where a similar trend of resistivity increase with decreasing diameter was reported for highly doped Si NWs (10^{19}–10^{20} cm^{-3}) is important to consider. In their work, they took into account the effect of charge located at the Si–SiO$_2$ interface and the associated depletion layer at the surface of the NW. This results in an effective core within the NW resulting in a reduced diameter for the conduction of the remaining bulk electrons (figure 6(a)). The accompanying model was based on the work of Schmidt *et al* where an effective diameter (D_E) can be defined based on standard material parameters as shown below, by solving Poisson's equation for a cylindrical wire [35]. In this present study, the vapour-phase ZnO NWs were transferred directly to an insulating substrate after growth without the assistance of an intermediate solvent or patterning technique to minimize the exposure to external sources of surface modification. This is particularly important for ZnO which is very surface sensitive as it has no intrinsic passivation layer as compared to Si. Furthermore, it should be noted that the detailed TEM measurements revealed that the NWs had smooth surfaces, free from the influence of roughness and corrugation [11]. However, the exact state of the surface at the atomic or molecular level is difficult to assess and can lead to potential variations in defect density, stoichiometry, and the density of adsorbed species, all of which will result in the modification of the local charge on the surface. For ZnO NWs, the increasing resistivity as the NW diameter diminishes can be explained by considering the influence of such charge trapped at the surface in terms of the model proposed by Schmidt *et al* for Si NWs and replacing the interface states by energy states associated with the free ZnO surface [35]. Under such conditions, the effective conduction diameter is given by the following expression

$$D_E = 2\sqrt{r^2 - \frac{2r\psi_0 N_{ss}}{N_d\left(1 + \frac{qr N_{ss}}{2\varepsilon_r \varepsilon_0}\right)}} \qquad (2)$$

where r is the NW radius, N_{ss} is the surface state density $(m^{-2} eV^{-1})$ and ψ_0 is the electrostatic potential at the surface, N_d is the doping concentration, q is the electronic charge, ε_r is the relative permittivity of the NW and ε_0 is the permittivity of free space. The measured resistivity (ρ_m) and the expected resistivity (ρ_e) are related by the following expression

$$\frac{\rho_m}{\rho_e} = \frac{(2r)^2}{D_E^2}. \tag{3}$$

The solid purple line in figure 6(b) depicts this model using the following parameters: bulk resistivity ($D \rightarrow \infty$) of 0.028 Ω cm to normalize the experimental results, $N_d = 1 \times 10^{18}$ cm^{-3}, a typical value for unintentionally doped vapour-phase NWs [11] and $N_{ss} = 0.9 \times 10^{12}$ cm^{-2} eV^{-1}, again a typical reported value for ZnO NWs [36]. This clearly depicts the trend of the data and the striking influence of surface states on the resistivity at small NW diameter. However, Björk *et al* found that this effect alone was not sufficient to explain the dependence of the measured resistivity for the differently doped Si NWs [34]. They attributed the additional effect to donor deactivation, which results from a dielectric mismatch with the surrounding medium (here it is vacuum). However, for the case of ZnO NWs, the results can be explained by the reduction of the conductive core alone. The effect of donor deactivation is not seen in our measurements, primarily due to the lower doping concentration of the ZnO NWs.

However, what is the origin of the variability seen in the measured resistivity at each diameter for the ZnO NWs in this paper? All of the NWs are deemed to be crystallographically similar with comparable surface morphologies which excludes a substantial variation in surface scattering behaviour [37, 38]. Instead, the origin of the variability in resistivity may lie with the random nature of species that bind to the reactive surface of the ZnO NWs, with the effect of this random nature becoming more prominent at the nanoscale. Alternatively, a variation in bulk doping concentration could produce the measured spread. These possibilities are considered below to uncover the major influence on the variation in NW resistivity.

The bare NWs, having been exposed only to air and without any other surface modification, will undoubtedly have chemisorbed and tightly bound species such as adsorbed ions of O_2^- and OH^- hydroxyls present on the surface. These groups induce surface states that act as electron traps removing charge carriers from the bulk as shown in figure 6(a). The density of the surface states varies between NWs, and a variation is even apparent in NWs of the same diameter and fabricated during the same growth batch [9, 36]. When placed in the vacuum system, most loosely bound species will desorb but a large proportion of tightly bound molecules will remain. The exact nature of this surface chemistry is expected to be somewhat unclear and hence will produce a variation in N_{ss} for the samples in this study. However, an important question is how sensitive is the resistivity to variations in N_{ss} for ZnO NWs? This can be gleaned in a simple manner by reference to equation (2). Figure 6(b) shows the resistivity of the experimental data,
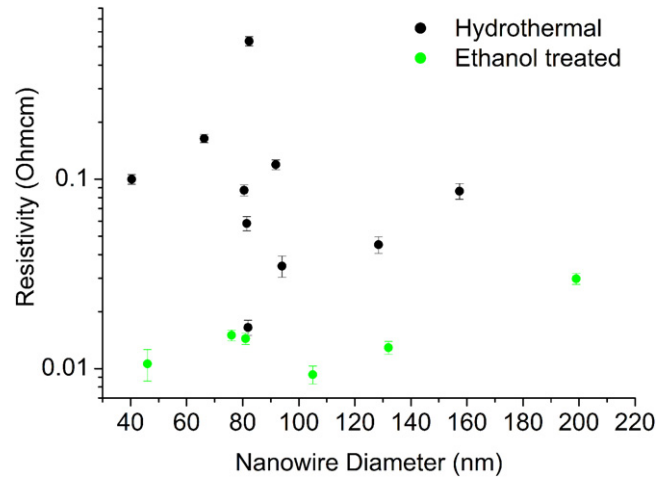
Figure 7. Plot of the measured NW resistivity of the 10 hydrothermal NWs (black) shown in figure 2 along with hydrothermal NWs that were exposed to ethanol (green).

normalized to 0.028 Ω cm, along with curves calculated from equation (2) based on a fixed doping concentration $N_d = 1 \times 10^{18}$ cm^{-3} and allowing N_{ss} to vary $(1.1 \pm 0.6) \times 10^{12}$ cm^{-2} eV^{-1}. The variation in the occupied surface state density between the two extremes bounds the experimental data and can account for the spread in resistivity. The values of N_{ss} used compare well in terms of order of magnitude to those measured on ZnO NWs by Soudi *et al* [36] although the exact values are smaller here as the NWs were measured in vacuum. However, it is important to consider bulk influences that are otherwise impossible to detect directly on the resistivity as possible mechanisms to account for the spread in measurements, including O vacancies, H incorporation, and low densities of low Z-number impurities or lattice anomalies. To discount this as a major factor, we demonstrate the removal of the scatter by neutralizing the effect of the surface states (electronic passivation). This was achieved by exposing six hydrothermal NWs from the same growth batch to ethanol and the results are presented in figure 7. The graph shows the resistivity of hydrothermal NWs with and without ethanol passivation. After exposure to ethanol an almost common datum of low resistivity and seemingly low dependence on NW diameter is achieved. Ethanol readily binds with the pristine ZnO surface [39] or with adsorbed species such as O ions [12]. In UHV, physisorbed ethanol desorbs at relatively low temperatures leaving a concentration of chemisorbed molecules at room temperature [40] which act as a reducing agent donating electrons at the surface [39] and decreasing the experimental resistivity as was predicted by Spencer *et al*. The reaction that occurs with adsorbed O ions has the effect of releasing charge trapped at such sites and eliminating the effect of the surface states and ensures $D_E = 2r$, effectively removing the dependence of the resistivity on NW diameter. The major reduction of the 10^2 spread in resistivity indicates that the variation of doping is not the dominant feature driving the variation in resistivity. Indeed, this result indicates that each treated NW has almost equivalent bulk electronic properties once the variable effect of the surface has been

removed, with the remaining experimental spread possibly associated with minor doping variations. The sensitivity of the resistivity to subtle variations in surface charge depicted here reinforces the interest in this material as an excellent detector.

4. Conclusions

We have shown the structural and electrical equivalence of individual ZnO NWs fabricated by vapour-phase (catalytic and non-catalytic) and hydrothermal techniques. Using an advanced four-probe STM the intrinsic resistivity of individual ZnO NWs has been extracted and shown to vary with diameter, a dependence that is rooted in the highly surface sensitive nature of ZnO. The variation in measured resistivity for similar diameter NWs is an intrinsic factor associated with small variations in the occupancy of surface states associated with adsorption of environmental species. As a result of the increased surface-to-volume ratio at the nanoscale, the surface state density, and their occupancy, has an exaggerated effect which can be used to detect environmental fluctuations through measurable variations in resistivity. The dominant role of the surface states and their random occupation through bonding of atmospheric species is confirmed by the subsequent passivation with ethanol. These results provide a much needed insight into the real resistivity of ZnO nanowires and show how a surface passivation technique can achieve a reproducible resistivity needed for the design of devices.

Acknowledgments

References

[1] Chu S, Wang G, Zhou W, Lin Y, Chernyak L, Zhao J, Kong J, Li L, Ren J and Liu J 2011 *Nature Nanotechnol.* **6** 506
[2] Wang Z L and Song J 2006 *Science* **312** 242
[3] Niepelt R, Schröder U C, Sommerfeld J, Slowik I, Rudolph B, Möller R, Seise B, Csaki A, Fritzsche W and Ronning C 2011 *Nanoscale Res. Lett.* **6** 511
[4] Léonard F and Talin A A 2011 *Nature Nanotechnol.* **6** 773
[5] Schlenker E, Bakin A, Weimann T, Hinze P, Weber D H, Gölzhäuser A, Wehmann H-H and Waag A 2008 *Nanotechnology* **19** 365707
[6] Chiu S-P, Lin Y-H and Lin J-J 2009 *Nanotechnology* **20** 015203
[7] He J H, Chang P H, Chen C Y and Tsai K T 2009 *Nanotechnology* **20** 135701
[8] Tsai L-T, Chiu S-P, Lu J G and Lin J-J 2010 *Nanotechnology* **21** 145202
[9] Zhang S, Hemesath E R, Perea D E, Wijaya E, Lensch-Falk J L and Lauhon L J 2009 *Nano Lett.* **9** 3268
[10] Hu Y, Liu Y, Xu H, Liang X, Peng L-M, Lam N, Wong K and Li Q 2008 *Phys. Chem.* C **112** 14225
[11] Hong W *et al* 2008 *Nano Lett.* **8** 950
[12] Zhang Q, Qi J, Huang Y, Li X and Zhang Y 2011 *Mater. Chem. Phys.* **131** 258
[13] Kind H, Yan H, Messer B, Law M and Yang P 2002 *Adv. Mater.* **14** 158
[14] Allen J E *et al* 2008 *Nature Nanotechnol.* **3** 168
[15] Bar-Sadan M, Barthel J, Shtrikman H and Houben L 2012 *Nano Lett.* **12** 2352
[16] Perea D E, Allen J E, May S J, Wessels B W, Seidman D N and Lauhon L J 2006 *Nano Lett.* **6** 181
[17] Stiegler J M, Tena-Zaera R, Idigoras O, Chuvilin A and Hillenbrand R 2012 *Nature Commun.* **3** 1131
[18] Yang P, Yan H, Mao S, Russo R, Johnson J, Saykally R, Morris N, Pham J, He R and Choi H-J 2002 *Adv. Funct. Mater.* **12** 323
[19] Ho S-T, Chen K-C, Chen H-A, Lin H-Y, Cheng C-Y and Lin H-N 2007 *Chem. Mater.* **19** 4083
[20] Hu H, Huang X, Deng C, Chen X and Qian Y 2007 *Mater. Chem. Phys.* **106** 58
[21] Park W, Hong W-K, Jo G, Wang G, Choe M, Maeng J, Kahng Y H and Lee T 2009 *Nanotechnology* **20** 475702
[22] Krivanek O L, Corbin G J, Dellby N, Elston B F, Keyse R J, Murfitt M F, Own C S, Szilagyi Z S and Woodruff J W 2008 *Ultramicroscopy* **108** 179
[23] Koch C 2002 *PhD Thesis* Arizona State University
[24] Makarovski A, Zhukov A, Liu J and Finkelstein G 2007 *Phys. Rev.* B **76** 161405(R)
[25] Lin X, He X B, Yang T Z, Guo W, Shi D X, Gao H-J, Ma D D D, Lee S T, Liu F and Xie X C 2006 *Appl. Phys. Lett.* **89** 43103
[26] Janotti A and Van de Walle C G 2009 *Rep. Prog. Phys.* **72** 126501
[27] Kisielowski C *et al* 2008 *Microsc. Microanal.* **14** 469
[28] Kirkham M, Wang X, Wang Z L and Snyder R L 2007 *Nanotechnology* **18** 365304
[29] Brewster M M, Zhou X, Lim S K and Gradečak S 2011 *Phys. Chem. Lett.* **2** 586
[30] Hofmann S, Sharma R, Wirth C T, Cervantes-Sodi F, Ducati C, Kasama T, Dunin-Borkowski R E, Drucker J, Bennett P and Robertson J 2008 *Nature Mater.* **7** 372
[31] Hartel P, Rose H and Dinges C 1996 *Ultramicroscopy* **63** 93
[32] Voyles P M, Grazul J L and Muller D A 2003 *Ultramicroscopy* **96** 251
[33] Van-Benthem K, Lupini A R, Oxley M P, Findlay S D, Allen L J and Pennycook S J 2006 *Ultramicroscopy* **106** 1062
[34] Björk M T, Schmid H, Knoch J, Riel H and Riess W 2009 *Nature Nanotechnol.* **4** 103
[35] Schmidt V, Senz S and Gösele U 2007 *Appl. Phys.* A **86** 187
[36] Soudi A, Hsu C-H and Gu Y 2012 *Nano Lett.* **12** 5111
[37] Khanal D R, Levander A X, Yu K M, Liliental-Weber Z, Walukiewicz W, Grandal J, Sánchez-Garciá M A, Calleja E and Wu J 2011 *J. Appl. Phys.* **110** 033705
[38] Hong W-K, Jo G, Kwon S-S, Song S and Lee T 2008 *IEEE Trans. Electron Devices* **55** 3020
[39] Spencer M J S, Wong K W J and Yarovsky I 2012 *J. Phys.: Condens. Matter* **24** 305001
[40] Kwak G and Yong K 2008 *J. Phys. Chem.* C **112** 3036